



An experimental determination of the effective oxygen diffusion coefficient for a high density polypropylene geomembrane

Michael G. Trefry and Bradley M. Patterson

CSIRO Land and Water
Technical Report 37/01, September 2001

**An experimental determination of the effective
oxygen diffusion coefficient for a high density
polypropylene geomembrane**

Michael G. Trefry and Bradley M. Patterson

CSIRO Land and Water, Private Bag No. 5

PO Wembley WA 6913, Australia

Technical Report 37/01

September 2001

Abstract

Laboratory experiments were performed to determine the effective oxygen diffusion coefficient for a polymer geomembrane. Such geomembranes are commonly employed to limit oxygen supply to reactive tailings deposits, thereby reducing acidification and other undesirable chemical transformations. The experiments used a simple chamber+membrane apparatus, together with an on-line oxygen sensor positioned within the chamber. Oxygen breakthrough curves, measured over several weeks for a high density polypropylene (HDPP) membrane, were fitted with a new analytical model parameterised by the membrane diffusion coefficient, chamber leakage and oxygen sensor consumption. The analytical model provided close fits to the data, and was also able to yield estimates of the oxygen consumption rate of the on-line sensor. The indicated value for the oxygen diffusion coefficient of the HDPP geomembrane was $4.6 \pm 1.3 \times 10^{-8} \text{ cm}^2 \text{ s}^{-1}$. This value was coupled with a simple physical model to deduce effective diffusion coefficients for composite HDPP-bentonite geosynthetic clay liners. The results show high sensitivity to bentonite water saturation, in line with earlier findings.

Introduction

The problem of managing the geochemical fates of reactive soils and industrial tailings is of global significance. For example, there are an estimated 12 million hectares of acid sulphate soils in the world [1], and in Canada alone there are 200 million tonnes of sulphidic industrial tailings [2]. Where possible, recent management plans for such reactive tailings involve emplacing the tailings in dewatered soil profiles and using geotechnical or other means to limit oxygen ingress to the tailings, thereby reducing acid production to levels deemed to be acceptable in an environmental sense. Single-material geoliners, e.g. liners consisting of soil, clay or synthetic materials, represent a useful technology for limiting supply of oxygen and other chemical compounds, and their physicochemical properties are reasonably well studied [3,4]. However these liners may be ineffective and costly, and there are still questions surrounding the ageing characteristics of the popular polymeric geomembranes [5], although their physical properties may be stable over the short to medium term [6]. When emplaced over a tailings facility, they act to reduce vertical oxygen fluxes to the tailings; the effect may be augmented by the intrinsic oxygen mineralisation characteristics of the surrounding soil profile.

In developing representative models of the reaction dynamics of sulphidic tailings facilities, quantifying the oxygen pathways and fluxes is critical. Where geomembranes are employed, numerical simulation becomes problematic due to the disparity in spatial and temporal scales between the dynamics in the thin geomembrane and the much larger tailings system. Special simulation techniques may be required and, accordingly, it is important to supply these techniques with accurate estimates of geomembrane properties. Recently, most interest was focused on the hydraulic properties of geomembranes [7-9], however gas permeability characteristics are now also salient [10-12]. This paper presents results of an experimental study of the diffusion characteristics of a polymer geomembrane used in an industrial site near Perth, Western Australia. Estimates of effective diffusion coefficient for

the geomembrane are obtained using a simple diffusion chamber apparatus, together with long-term on-line monitoring of oxygen concentration and nonlinear regressions.

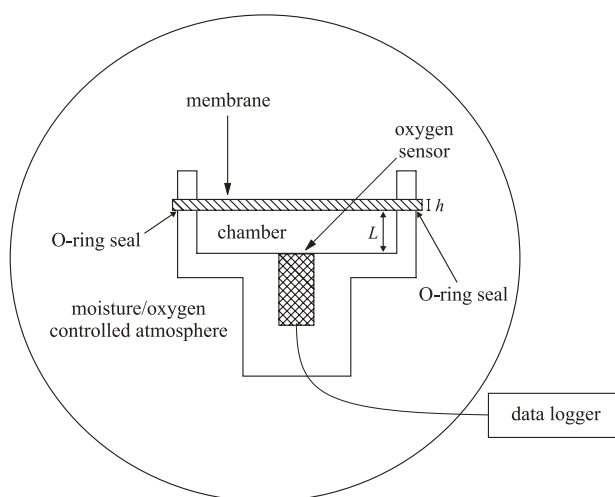


Figure 1: Schematic of the diffusion chamber apparatus. The cylindrical chamber+membrane assembly is shown in cross section. The assembly is immersed in a controlled atmosphere and connected to an external data logger.

Experimental Apparatus and Methods

An apparatus was constructed to determine the flux rate of oxygen through different membrane materials. The materials considered were stainless steel (hereafter referred to as the metal membrane) and a high density polypropylene (HDPP) membrane. A schematic of the apparatus is shown in Fig. 1. The apparatus was constructed from thick acrylic plastic (polymethylmethacrylate) with a Figaro oxygen sensor (KE 25) countersunk so the sensor was flush with the base of the gas chamber. The gas chamber volume was $18.3 \pm 0.3 \text{ cm}^3$ (gravimetrically determined), with an exposed surface area to the atmosphere of $38.5 \pm 0.5 \text{ cm}^2$. The chamber depth was $0.48 \pm 0.05 \text{ cm}$. A gas-tight seal between the gas chamber and the material tested was constructed using a viton O-ring. The apparatus and membrane

materials were stored anaerobically for 1 to 2 weeks prior to experiments, which were carried out at room temperature.

For the experiments either a 1.0 mm thick stainless steel sheet or a 0.75 ± 0.15 mm thick HDPP sheet (Nylex Millennium polypropylene) was attached to the apparatus under anaerobic conditions, and then the apparatus was exposed to an aerobic (21% oxygen) atmosphere. In both experiments (metal and HDPP), oxygen sensor response data were collected at 2 min intervals and stored using a CSIRO data logger.

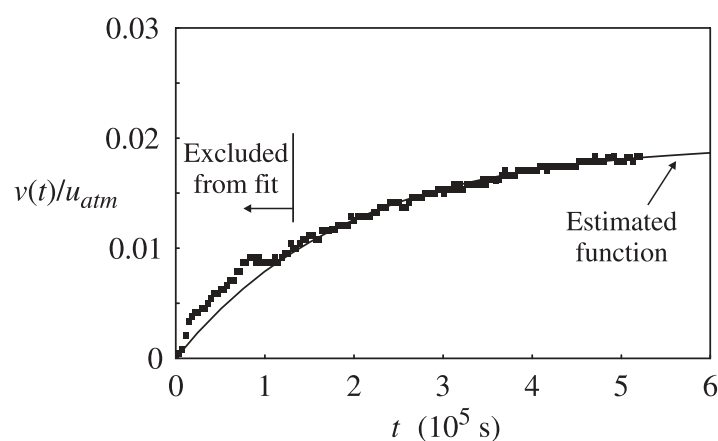


Figure 2: Breakthrough data (squares) and least-squares estimate curve (solid line) for the metal membrane experiment. For clarity, only every 30th data point is shown. The first 1099 data points were excluded from the regression.

Analysis of Results

Development of the Breakthrough Model

Figures 2 and 3 show oxygen breakthrough curves measured in the enclosed chamber for the cases where the membrane is impervious (metal membrane, Fig. 2), and permeable (HDPP membrane, Fig. 3). All chamber concentrations, denoted by v , are normalized by the external atmospheric equilibrium concentration, denoted by u_{atm} . All ordinate axes are normalized with respect to atmospheric oxygen concentrations. Figures 2 and 3 show almost

immediate breakthroughs of oxygen into the chamber. The long time scale of equilibration is important, as is the fact that in both

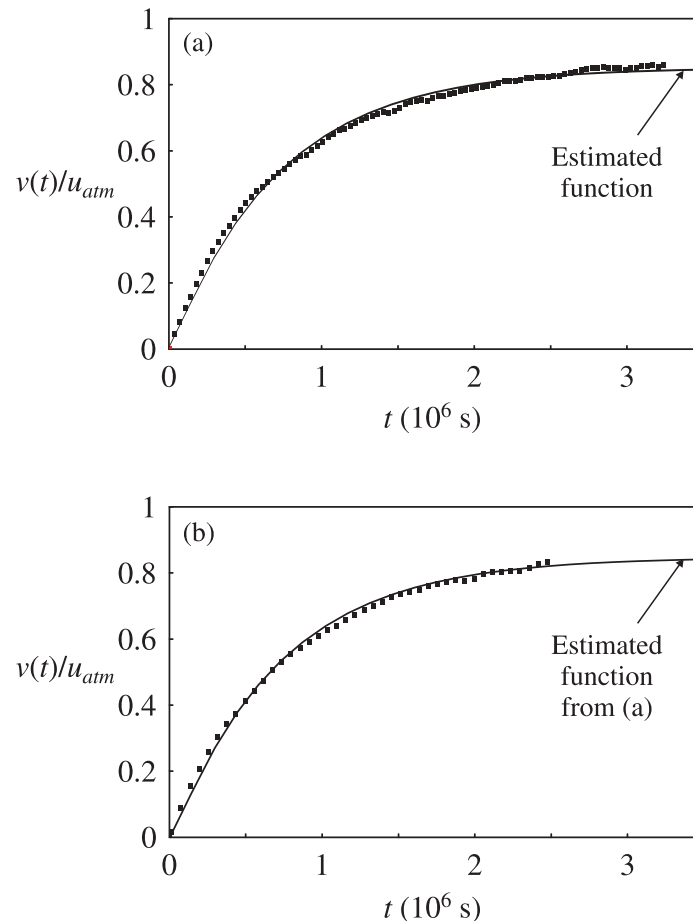


Figure 3: Breakthrough data (squares) and least-squares estimate curve (solid line) for two HDPP membrane experiments. For clarity, only every 200th data point is shown. Part (a) shows data and fitted curve for a five-week experiment, while part (b) shows data for a separate three-week experiment together with the fitted curve from part (a).

experiments the equilibrium chamber concentration is less than atmospheric concentration. These observations indicate that the breakthrough curves embody effects associated with (i) oxygen flux through the membrane (taken to be zero for the metal membrane experiment), (ii) a lumped “leakage” flux representing the combined effect of all other pathways by which oxygen may enter the chamber, and (iii) an oxygen loss mechanism due to consumption by the sensor. While these fluxes and rates are very low, as is evidenced by the long

equilibration times of the breakthrough curves, the rate of diffusive redistribution of oxygen once it is inside the chamber is relatively rapid and the oxygen concentration in the chamber can be regarded as well-mixed.

Appendix A presents a model of breakthrough dynamics based on this well-mixed chamber approximation. The resulting breakthrough function (eq A.16) is parameterised by a group of *transport* parameters – the membrane diffusion coefficient, D , the leakage rate parameter, r , and the sensor consumption rate, s – as well as two *geometric* parameters – the membrane thickness, h , and chamber length, L . A feature of the breakthrough function is that for low D , zero r and large h the breakthrough is significantly delayed. A drawback of the model is that it is physically ill-posed, in that the leakage and membrane diffusion terms are closely related. Greatest discrimination between these fluxes occurs where membrane breakthrough is slow (i.e. where membrane thickness is large and diffusion coefficient is small), in which case early chamber breakthroughs may be attributed to leakage.

Unfortunately, the oxygen sensor is least accurate for small concentrations in the vicinity of the detection limit, which may lead to difficulty in correctly apportioning the observed chamber influx between the membrane diffusion and chamber leakage processes.

Mathematically, this ill-posed behaviour is manifested in the presence of a number of feasible, if not always realistic, extrema in the least-squares objective function used in regressions of the breakthrough function against measured data. Fortunately, existing literature values may be used as a guide in choosing the appropriate extremum.

Nonlinear Regression Methodology

In principle, the breakthrough function permits simultaneous estimation of the effective membrane diffusion coefficient and the leakage and consumption rates. In practice this was achieved by the following numerical means. First, the evaluation of the breakthrough function $v(t)/u_{atm}$ was automated by employing a Newton-Raphson method [13] over an irregular grid to locate the first twenty pole points α_n . In practice, only ten poles were

required due to the rapidly convergent nature of the summation for $t > 0$ in eq (A.16). Then, this numerical breakthrough function was coupled to the experimental data in a least-squares objective function, which was minimised using a standard nonlinear regression routine. All calculations were performed with double precision Fortran arithmetic in order to maintain acceptable precision, especially in the determination of pole points (the Fortran code is available from the authors on request). The on-line nature of the oxygen sensor provided many breakthrough data points at negligible cost, leading to excellent statistics in the regressions. Confidence intervals for the p estimated parameters over n data points were constructed using the general linear approximation

$$|\theta_i - \hat{\theta}_i| \leq \sqrt{P_{ii}} t_{n-p, \alpha/2} \quad (1)$$

where $\hat{\theta}_i$ is the least-squares estimate of parameter θ_i , $\sqrt{P_{ii}}$ is the square root of the i -th diagonal of the asymptotic covariance matrix and estimates the asymptotic parameter standard error σ_i , and $t_{n-p, \alpha/2}$ is the upper $\alpha/2$ quantile for the t -distribution with $n-p$ degrees of freedom.

Precision of Regressions

In this section the size of uncertainty measures for the nonlinear regressions are explored for each of the three experiments for fixed (mean) values of the geometric quantities h and L . For the metal membrane experiment, D was assumed to be zero and the breakthrough curve of eq (A.18) was fitted to the data. The purpose of this was to gain an approximate estimate of the leakage rate r for the Viton ring seal method, which is used in both metal and HDPP membrane experiments. Figure 2 shows that at early times the breakthrough data (squares) are noisy, which may be due to two effects. Firstly, the oxygen sensor may experience detection limit problems for such low concentration levels. Secondly, the raw sensor voltage output is converted to oxygen concentrations using a single calibration

curve determined as a best fit over the range from non-detect to atmospheric oxygen concentration. This best-fit curve is most accurate for higher concentrations. Accordingly, the first 1100 data points of the breakthrough curve were ignored during the least-squares process, leaving 3245 points for regression. Table 1 shows that the 95% confidence intervals on the resulting r and s parameters are extremely tight. The corresponding breakthrough curve is also drawn on Fig. 2 (solid line), showing good agreement with the measured data.

Membrane	Degrees of Freedom (n,p)	D ($\text{cm}^2 \text{ s}^{-1}$)	r (10^{-7} s^{-1})	s (10^{-7} s^{-1})
Metal Eq (A.18)	(3245,2)	-	1.01 ± 0.00	50.71 ± 0.21
HDPP Eq (A.16)	(D,s) (D,r,s) (27359,2) (27359,3)	$4.49 \pm 0.01 \times 10^{-8}$ $3.82 \pm 0.09 \times 10^{-9}$	0.00^a 11.5 ± 0.0	2.18 ± 0.01 2.14 ± 0.01

Table 1: Estimated transport parameter values D , r and s for the two experiments. Reduced-parameter regressions for HDPP are explained in the text. Linear 95% confidence intervals are supplied for each parameter estimate. ^a Value held constant.

For the HDPP experiment all three parameters (D,r,s) may be non-zero. Several regression methods were used. Performing a single parameter fit for D with r and s fixed at the metal experiment values resulted in an unacceptably poor result (not shown). As an alternative, the problem was reduced to a two-parameter regression as follows. Since the viton O-ring is in contact with the HDPP membrane at the seal, it is assumed that under mechanical pressure against the rigid chamber structure the seal will effectively act as a compressed HDPP membrane. Thus, the leakage rate r is assumed to be zero, with all flux into the chamber attributed to diffusion through the HDPP membrane. In this way, the problem is reduced to a regression over the D and s parameters. As a final alternative, a full three-parameter regression was attempted directly. Table 1 gives results for these various

regressions for the HDPP experiment. Again, the confidence intervals are tight, as is evidenced by the close agreement between the two- and three-parameter fit curves and the measured data (see Fig. 3). Figure 3 also shows the identical two-parameter best-fit curve plotted against a repeat of the HDPP experiment over a shorter time.

Agreement is reassuringly close, although the parameter estimates for the different regressions show interesting trends. Table 1 shows that the fitted sensor consumption rates, s , are similar for the two- and three-parameter regressions, at approximately $2.15 \pm 0.05 \times 10^{-7} \text{ s}^{-1}$. However, the D coefficients for HDPP differ by an order of magnitude, with inclusion of the leakage term in the regression leading to a much smaller diffusion coefficient, being similar to a value recently reported for an acrylic polymer [14]. The fitted values of D of $4.5 \times 10^{-8} \text{ cm}^2 \text{ s}^{-1}$ (two parameter fit) and $3.8 \times 10^{-9} \text{ cm}^2 \text{ s}^{-1}$ (three parameter fit) may be compared with literature values. Electrochemical [15] and luminescence-quenching [16,17] studies indicate the typical range 10^{-8} to $10^{-6} \text{ cm}^2 \text{ s}^{-1}$ for oxygen diffusion coefficients in various polymers. In a study related to food packaging, *Dibelo et al.* [18] found a value for the oxygen diffusion coefficient of standard-density polypropylene films of $2.9 \times 10^{-8} \text{ cm}^2 \text{ s}^{-1}$, and *Eken et al.* [19] reported values ranging from 0.9 to $7.2 \times 10^{-7} \text{ cm}^2 \text{ s}^{-1}$ for γ -irradiated polypropylene films. However, for HDPE, *Epacher et al.* [20] supplies a series of references dating from 1961 supporting a value of $1.7 \times 10^{-7} \text{ cm}^2 \text{ s}^{-1}$, which is significantly higher than the value for standard density polypropylene from *Dibelo et al.* [18]. *Van Krevelen* [21] provides activation energies for polypropylene, which may be used in an Arrhenius relation to obtain a range of 0.67 to $8.1 \times 10^{-7} \text{ cm}^2 \text{ s}^{-1}$ for the oxygen diffusion coefficient. On this basis, the three-parameter estimate for D (and thus for r) may be rejected as being unreasonably low, probably due to the common parameterisation of the diffusion and leakage terms mentioned earlier. The two-parameter estimate lies just below the range indicated by *van Krevelen* (21), but higher than the value of *Dibelo et al.* [18]. Hence the two-parameter estimate ($4.5 \times 10^{-8} \text{ cm}^2 \text{ s}^{-1}$) is congruent with previous analyses and is taken as representative

for HDPP in this experiment. Also, the table shows that the sensor consumption rate in the HDPP experiment is twenty-five times lower than in the metal experiment. This may signify that the first-order consumption model is inaccurate over the full concentration range encountered in the metal and HDPP experiments. It is held that the sensor consumption rate value $2.15 \pm 0.05 \times 10^{-7} \text{ s}^{-1}$ is representative for normalized oxygen concentrations of the order of unity, i.e. at atmospheric oxygen concentrations.

Experiment	Transport Parameter	Varying L	Varying h	Varying L, h
HDPP	D ($10^{-8} \text{ cm}^2 \text{ s}^{-1}$) s (10^{-7} s^{-1})	$L \in (4.43, 5.11)$ (4.21, 4.80) (2.20, 2.16)	$h \in (0.60, 0.90)$ (3.53, 5.49) (2.12, 2.23)	(3.31, 5.86) (2.11, 2.26)

Table 2: Effect of geometric parameter uncertainty on least-squares estimates of the transport parameters D , r and s for the HDPP experiment. Three-parameter regressions were performed using L and h at the extrema of their measurement uncertainties to obtain absolute error measures for the transport parameters.

Influence of Uncertainty in the Geometric Parameters

The previous section demonstrated that the proposed breakthrough model was able to reproduce the features of the observed HDPP data reasonably precisely, with the large numbers of data points contributing to tight confidence intervals in the least-squares estimates for the transport parameters. Unfortunately, the true error measures for the experiments are more substantial. Absolute measurement error in the chamber length parameter, L , is estimated at 5%, whilst typical tolerances for polymer assemblies are between 10 and 20%. In order to account for the effects of these uncertainties, HDPP regressions were carried out over the full range of geometric parameter values, taken individually and together. Results are presented in Table 2 for the HDPP experiment. Note that for the last column in the table, the quoted parameter ranges were determined from the four corner points of the

$(L_{\min}, L_{\max}) \times (h_{\min}, h_{\max})$ region and the individual parameter ranges (previous columns). Due to the nonlinearity in these parameters of the least-squares objective function, these ranges may not truly represent the full range of transport parameter values over the geometric region. Mapping the true intervals is computationally expensive, so Table 2 contains the eight-point approximations to the intervals.

For the HDPP experiment, the regressions show that D is sensitive to the variations in membrane thickness h , but not to the variations in chamber length L , while s is insensitive to changes in h and L . Allowing h and L to vary simultaneously makes little difference to the intervals calculated by varying h alone, with the uncertainty in D estimated at approximately 30% for this experiment. The recommended oxygen diffusion coefficient value for HDPP is $4.6 \pm 1.3 \times 10^{-8} \text{ cm}^2 \text{ s}^{-1}$. These geometric uncertainties are not unreasonable, especially considering that practical field geomembranes must be fabricated to cover areas of tens of hectares or more. In such circumstances it would be unlikely that finer fabrication tolerances could be met.

Composite Bentonite-HDPP Geomembranes

Composite liners are specially fabricated to impede specific compounds. For example, a composite liner comprising a thin polymer layer and a thicker clay layer may impede oxygen flux whenever the clay is at least partially saturated. When emplaced over a tailings facility, they act to reduce vertical oxygen fluxes to the tailings; the effect may be augmented by the intrinsic oxygen mineralisation characteristics of the surrounding soil profile. Here the effective diffusion coefficient for a composite bentonite-HDPP geoliner is considered. In particular, data for a Bentofix 2000X bentonite-impregnated membrane ($7.2 \pm 1.4 \text{ mm}$ thick, porosity 0.6 ± 0.05 , density $1.17 \pm 0.05 \text{ g cm}^{-3}$) are used. Of critical importance is the saturation state of the bentonite. Higher water saturations lead to smaller diffusion coefficients. *Didier et al.* [11] show that moderate variations in bentonite water content can

lead to variations in permeability of several orders of magnitude, while *Aubertin et al.* [10] use an empirical tortuosity formulation to map the variation of diffusion coefficient with water saturation. Their model reduces to

$$D_{bentonite} = D_a^{mol} \frac{\theta_a^{2x+2}}{n^2} + K_H D_w^{mol} \frac{\theta_w^{2y+2}}{n^2} \quad (2)$$

where the water saturation $S = \theta_w/n = (n - \theta_a)/n$ is expressed in terms of the volumetric bentonite air and water fractions θ_a and θ_w , and the porosity n . K_H is Henry's coefficient (0.03), and the molecular oxygen diffusion coefficients in air and water are assumed to be [10] $D_a^{mol} = 1.8 \times 10^{-1} \text{ cm}^2 \text{ s}^{-1}$ and $D_w^{mol} = 2.5 \times 10^{-5} \text{ cm}^2 \text{ s}^{-1}$, respectively. The exponents x and y are found to lie in the range 0.6 to 0.75, and may be assumed to be equal. Figure 4 shows that the bentonite diffusion coefficient decreases by three orders of magnitude as water saturation changes from 0 to 1, and is approximately $10^{-6} \text{ cm}^2 \text{ s}^{-1}$ when fully saturated. The quoted uncertainties in porosity yield variations of similar sizes to those for the exponent ranges in Fig. 4.

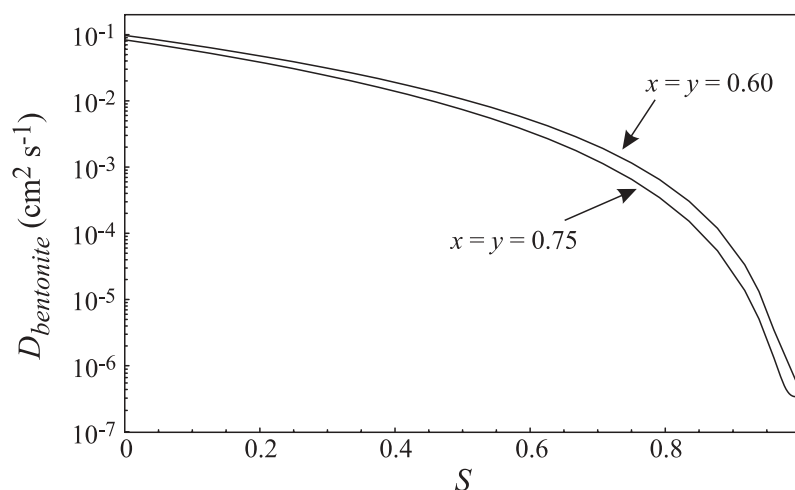


Figure 4: Variation of bentonite diffusion coefficient with water saturation S . Curves are shown for the representative range of tortuosity exponent x ($= y$).

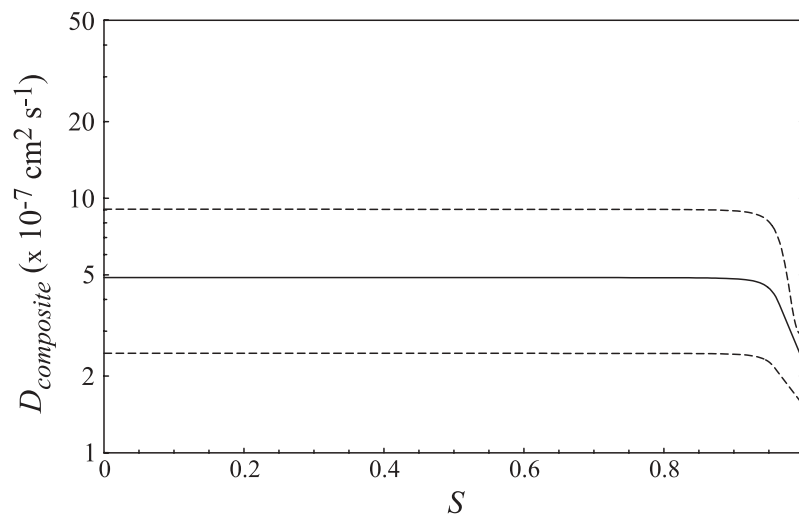


Figure 5: Variation of the composite diffusion coefficient with water saturation S . The solid line shows the mean estimate, while the dashed lines represent the bounds of the experimental accuracy, based on absolute measurement errors.

The asymptotic (lower bound) diffusion coefficient for the bentonite membrane is thus at least an order of magnitude higher than the HDPP value, but the usually greater thickness of the bentonite membrane will improve its performance as an oxygen barrier. The contributions of the bentonite and HDPP layers to the effective liner diffusion coefficient can be estimated using the parallel relationship [22, p.47]

$$\frac{h_{composite}}{D_{composite}} = \frac{h_{HDPP}}{D_{HDPP}} + \frac{h_{bentonite}}{D_{bentonite}} \quad (3)$$

where $h_{composite} = h_{HDPP} + h_{bentonite}$. With the mean values $h_{composite} = 7.95$ mm, $h_{HDPP} = 0.75$ mm, $h_{bentonite} = 7.2$ mm together with the recommended value for D_{HDPP} and the tortuosity model of *Aubertin et al.* [10], leads to estimated values for the diffusion coefficient of oxygen in the composite geomembrane as shown in Fig. 5 (solid line). An obvious result is that unless the bentonite saturation is very high (≈ 1), the bentonite layer does not materially influence the diffusion coefficient of the composite sheet, as has been established elsewhere [10]. The dashed lines in Fig. 5 show the absolute variation in the estimated value due to uncertainties in the geometric parameters, in D_{HDPP} and the x and y exponents.

Summary

In summary, experimental diffusion data was interpreted in terms of a chamber breakthrough model parameterized by membrane diffusion coefficient, sensor consumption and chamber leakage. It was found that the membrane diffusion and chamber leakage were mathematically dependent, leading to inaccurate estimates for the associated parameters during regressions. Eliminating the chamber leakage parameter from the regressions yielded a diffusion coefficient for HDPP in line with literature values. As a by-product of the regressions, the intrinsic oxygen consumption rate of a popular electrochemical sensor was also determined. Major contributions to uncertainty of these oxygen diffusion coefficients arise from uncertainties in the geometric parameters of the experiment, e.g. membrane thickness and chamber length. Taking these into account leads to reasonably accurate effective diffusion coefficients for the HDPP material. These values were applied to a simple composite diffusion model to gain estimates of the effective diffusion coefficient for a composite HDPP-bentonite geosynthetic clay liner. This model highlights the sensitivity of the composite geoliner diffusion coefficient to bentonite water saturation. For most saturations less than unity, $D_{bentonite}$ is high, and the composite diffusion coefficient is approximately equal to the $D_{HDPP} \times h_{bentonite}/h_{HDPP}$. Only at the highest saturations does the decline in $D_{bentonite}$ lead to reductions in $D_{composite}$.

Acknowledgements

This work was part funded by WMC Resources Ltd.

Appendix A – Detailed Breakthrough Model

The problem of a one-dimensional slab (i.e. the barrier in the present context) in contact with a well-mixed chamber is considered, using the approach of *Carslaw and Jaeger* [23, pp. 311-313]. Concentrations in the slab and chamber are denoted $u(x,t)$ and $v(t)$, respectively. The slab, of thickness h and initially at zero concentration, is in contact at $x = 0$ with constant (atmospheric) concentration u_{atm} and at $x = h$ with a well-mixed chamber (length L and cross section A) initially at zero concentration. The slab (barrier) diffusion coefficient is D . Oxygen diffuses through the slab into the chamber, and the chamber concentration is affected by other source (leakage) and sink (sensor consumption) terms. Leakage is modeled as a diffusive process, with leakage flux proportionate to the difference in concentration between the chamber and the external atmosphere. The leakage rate constant is r . Similarly, the consumption dynamics of the electrochemical sensor are represented by a first-order term with rate constant s . Physically, this describes a sensor that utilizes oxygen in proportion to the local oxygen concentration, i.e. at low concentrations only small amounts of oxygen are consumed per unit time, and at high concentrations higher amounts are consumed per unit time. No analytical solutions for this system are extant in the literature. The equations governing the dynamics are

$$\frac{\partial u}{\partial t} = D \frac{\partial^2 u}{\partial x^2} ; u(x,0) = 0 ; u(0,t) = u_{atm} \quad (\text{A.1})$$

$$AL \frac{dv}{dt} = -AD \left. \frac{\partial u}{\partial x} \right|_{x=h} + rAL(v_{atm} - v) - sALv ; v(0) = 0 \quad (\text{A.2})$$

As only the effective diffusion coefficient of the barrier is of interest, partitioning effects are neglected (see ref. 24 for a similar application involving partitioning) and the equation system is completed by specifying continuity relationships between u and v , i.e.

$$u(h,t)=v(t) ; u_{atm}=v_{atm} \quad (\text{A.3})$$

The solution of the equation system proceeds by substituting eq (A.3) into (A.2), and taking Laplace transformations [25] of eqs (A.1) and (A.2), yielding

$$p\bar{u}=D\frac{d^2\bar{u}}{dx^2} \quad \text{subject to } \bar{u}(0)=u_{atm}/p \quad (\text{A.4})$$

$$pL\bar{u}(h)=-D\left.\frac{d\bar{u}}{dx}\right|_{x=h} -L(s+r)\bar{u}(h)+Lru_{atm}/p \quad (\text{A.5})$$

where $\bar{u}(x)$ is the Laplace transformation of $u(x,t)$. In this notation, $\bar{u}(x)$ has implicit dependence on the transformation variable p . For $D \neq 0$, the solution of eq (A.4) is

$$\bar{u}(x)=B\sinh qx + \frac{u_{atm}}{p}\cosh qx \quad (\text{A.6})$$

with $q^2 = p/D$. The integration constant B is fixed by satisfying eq (A.5), yielding, after algebra,

$$\bar{u}(x)=\frac{u_{atm}}{p}\frac{Dq\cosh q(x-h) - L(p+r+s)\sinh q(x-h) + Lr\sinh qx}{L(p+r+s)\sinh qh + Dq\cosh qh} \quad (\text{A.7})$$

In order to recover the temporal solution $u(x,t)$, it remains to perform the inverse Laplace transformation on eq (A.7). This is most easily accomplished by invoking the Inversion Theorem [23, p. 302], which states

$$u(x,t)=\frac{1}{2\pi i}\oint_{\Gamma}e^{pt}\bar{u}(x)dp \quad (\text{A.8})$$

where Γ is a contour in the complex plane chosen large enough to ensure that it encloses all poles of the integrand. With this choice, and using convergence properties of the integrand for large p , eq (A.8) reduces via the Residue Theorem to [26, p. 403]

$$u(x,t) = \sum_n \text{Res}(e^{pt} \bar{u}(x)) \quad (\text{A.9})$$

where the summation is over all the poles of the integrand, and $\text{Res}(\)$ is the residue operator.

The poles are most easily identified by making the transformation $q = i\alpha$, and thus

$p = -D\alpha^2$. Eq (A.7) then becomes

$$\bar{u}(x) = -\frac{u_{atm}}{D\alpha^2} \frac{Lr \sin \alpha x - L(r+s-D\alpha^2) \sin \alpha(x-h) + D\alpha \cos \alpha(x-h)}{D\alpha \cos \alpha h + L(r+s-D\alpha^2) \sin \alpha h} \quad (\text{A.10})$$

Poles occur at $\alpha = 0$, and where

$$D\alpha \cos \alpha h + L(r+s-D\alpha^2) \sin \alpha h = 0 \quad (\text{A.11})$$

or, equivalently,

$$\tan \alpha h = \frac{-D\alpha}{L(r+s-D\alpha^2)} \quad (\text{A.12})$$

The roots of eq (A.12) are transcendental and form a denumerably infinite set of pole points $\{\alpha_n\}$, $n=1,2,\dots$. They are easily determined numerically for given values of the system parameters D , h , r , s , L . It remains to calculate the residues of eq (A.7) at the pole points. This often laborious task is facilitated through the use computer algebraic techniques.

Consider the (steady state) pole at $\alpha = 0$. This can be shown to be a simple pole and, hence, the corresponding residue is

$$\lim_{p \rightarrow 0} p e^{pt} \bar{u}(x) = \frac{u_{atm} \{D + L[rh + s(h-x)]\}}{D + L(r+s)h} \quad (\text{A.13})$$

For the n -th pole at $p = -D\alpha_n^2$, the integrand of eq (A.7) may be expressed as $g(p)/h(p)$ where $h(-D\alpha_n^2) = 0$, but neither g nor h' are zero at the pole. Therefore [26, p. 213] the residue at the pole is given by $g(-D\alpha_n^2)/h'(-D\alpha_n^2)$. In this way the residue of the integrand of eq (A.7) at the pole $p = -D\alpha_n^2$ can be shown to be

$$\frac{-2Du_{atm}e^{-D\alpha_n^2 t}}{\sin \alpha_n h} \times \left\{ \frac{Lr \sin \alpha_n x - L(r+s) \sin \alpha_n (x-h) + D\alpha_n [\cos \alpha_n (x-h) + L\alpha_n \sin \alpha_n (x-h)]}{D\alpha_n^2 [Dh\alpha_n^2 L^2 - 2(r+s)hL^2 + D(L+h)] + L(r+s)[D + L(r+s)h]} \right\} \quad (\text{A.14})$$

Hence, summing the residue (A.13) with the infinite set of residues (A.14), and applying eq (A.11), the concentration distribution in the barrier slab is

$$u(x,t) = \frac{u_{atm} \{D + L[rh + s(h-x)]\}}{D + L(r+s)h} - 2Du_{atm} \sum_{n=1}^{\infty} \frac{e^{-D\alpha_n^2 t}}{\sin \alpha_n h} \times \left\{ \frac{Lr \sin \alpha_n x - L(r+s) \sin \alpha_n (x-h) + D\alpha_n [\cos \alpha_n (x-h) + L\alpha_n \sin \alpha_n (x-h)]}{D\alpha_n^2 [Dh\alpha_n^2 L^2 - 2(r+s)hL^2 + D(L+h)] + L(r+s)[D + L(r+s)h]} \right\} \quad (\text{A.15})$$

The quantity measured in the experiment is $v(t)$, the chamber concentration, which, by eq (A.3), is finally

$$\frac{v(t)}{v_{atm}} = \frac{u(h,t)}{u_{atm}} = \frac{(D + Lrh)}{D + L(r+s)h} - 2D \sum_{n=1}^{\infty} \frac{e^{-D\alpha_n^2 t}}{\sin \alpha_n h} \times \left\{ \frac{D\alpha_n + Lr \sin \alpha_n h}{D\alpha_n^2 [Dh\alpha_n^2 L^2 - 2(r+s)hL^2 + D(L+h)] + L(r+s)[D + L(r+s)h]} \right\} \quad (\text{A.16})$$

If the barrier is impermeable, $D = 0$, the above expression does not hold. In this case u is everywhere zero and the dynamical equation for the chamber concentration is

$$\frac{dv}{dt} = r(v_{atm} - v) - sv \quad ; \quad v(0) = 0 \quad (\text{A.17})$$

which is easily integrated to yield

$$\frac{v(t)}{v_{atm}} = \frac{r}{r+s} \left(1 - e^{-(r+s)t}\right) \quad (\text{A.18})$$

References

1. Bronswijk, J. J. B., Nugroho, K., Aribawa, I. B., Groenenberg, J. E., and Ritsema, C. J., Modeling of oxygen-transport and pyrite oxidation in acid sulfate soils, *J. Environ. Qual.* 22(3), 544-554, 1993.
2. Yanful, E. K., Simms, P. H., and Payant, S. C., Soil covers for controlling acid generation in mine tailings: A laboratory evaluation of the physics and geochemistry, *Water Air Soil Poll.* 114(3-4), 347-375, 1999.
3. Aminabhavi, T. M., and Naik, H. G., Chemical compatibility testing of geomembranes – sorption/desorption, diffusion and swelling phenomena, *Geotext. Geomembranes* 16(6), 333-354, 1998.
4. Simms, P. H., and Yanful, E. K., Some insights into the performance of an experimental soil cover near London, Ontario, *Canad. Geotech. J.* 36(5), 846-860, 1999.
5. Vink, P., and Fontijn, H. F. N., Testing the resistance to oxidation of polypropylene geotextiles at enhanced oxygen pressures, *Geotext. Geomembranes* 18(5), 333-343, 2000.
6. Eith, A. W., and Koerner, G. R., Assessment of HDPE geomembrane performance in a municipal waste landfill double liner system after eight years of service, *Geotext. Geomembranes* 15(4-6), 277-287, 1997.
7. Shackelford, C. D., Benson, C. H., Katsumi, T., Edil, T. B., and Lin, L., Evaluating the hydraulic conductivity of GCLs permeated with non-standard liquids, *Geotext. Geomembranes* 18(2-4), 133-161, 2000.

8. Cazaux, D., and Didier, G., field evaluation of hydraulic performances of geosynthetic clay liners by small and large-scale tests, *Geotext. Geomembranes* 18(2-4), 163-178, 2000.
9. Fox, P. J., De Battista, D. J., and Mast, D. G., Hydraulic performance of geosynthetic clay liners under gravel cover soils, *Geotext. Geomembranes* 18(2-4), 179-201, 2000.
10. Aubertin, M., Aachib, M., and Authier, K., Evaluation of diffusive gas flux through covers with a GCL, *Geotext. Geomembranes* 18(2-4), 215-233, 2000.
11. Didier, G., Bouazza, A., and Cazaux, A., Gas permeability of geosynthetic clay liners, *Geotext. Geomembranes* 18, 235-250, 2000.
12. Shan, H.-Y., and Yao, J.-T., Measurement of air permeability of geosynthetic clay liners, *Geotext. Geomembranes* 18, 251-261, 2000.
13. Mathews, J. H., *Numerical Methods for Mathematics, Science and Engineering*, Second Edition, Prentice Hall: New Jersey, 1992, p.84.
14. Katircioglu, T. Y., Kaptan, H. Y., and Guven, O., Determination of oxygen diffusion coefficient of poly(methacrylonitrile) II and the calculation of diffusion activation energy, *J. Appl. Polymer Sci.* 74, 1108-1118, 1999.
15. Haug, A. T., and White, R. E., Oxygen diffusion coefficient and solubility in a new proton exchange membrane, *J. Electrochem. Soc* 147(3), 980-983, 2000.
16. Rharbi, Y., Yekta, A., and Winnik, M. A., A method for measuring oxygen diffusion and oxygen permeation in polymer films based on fluorescence quenching, *Anal. Chem.* 71, 5045-5053, 1999.
17. Jayarajah, C. N., Yekta, A., Manners, I., and Winnik, M. A., Oxygen diffusion and permeability in alkylaminothionylphosphazene films intended for phosphorescence barometry applications, *Macromolecules* 33, 5693-5701, 2000.

18. Dibelo, P. M., Manganaro, J. L., and Aguinaldo, E. R., *Encyclopedia of Chemical Technology*, (M. Howe-Grant, Ed.), Fourth Edition, John Wiley: New York, 1991, vol. 3, p.938.
19. Eken, M., Turhan, Ş., Kaptan, Y., and Güven, O., Diffusion of oxygen into irradiated polypropylene films, *Radiat. Phys. Chem.* 46(4-6), 809-812, 1995.
20. Epacher, E., Tolvéth, J., Kröhnke, C., and Pukánszky, B., Processing stability of high density polyethylene: effect of adsorbed and dissolved oxygen, *Polymer* 41(23), 8401-8408, 2000.
21. Van Krevelen, D. W., *Properties of Polymers*, Third Edition, Elsevier: Amsterdam, 1997, pp.548-551.
22. Crank, J., *The Mathematics of Diffusion*, Second Edition, Clarendon: Oxford, 1975, 414pp.
23. Carslaw, H. S., and Jaeger, J. C., *Conduction of Heat in Solids*, Second Edition, Clarendon: Oxford, 1959, 510pp.
24. Paul, D. R., and DiBenedetto, A. T., Diffusion in amorphous polymers, *J. Polymer Sci. C10*, 17-44, 1965.
25. Bellman, R. E., and Roth, R. S., *The Laplace Transform*, World Scientific: Singapore, 1984, 158pp.
26. Marsden, J. E., *Basic Complex Analysis*, Freeman: San Francisco, 1973, 472pp.